Proceedings of the ASME 2017 12th International Manufacturing Science and Engineering Conference
MSEC 2017
June 4-8, 2017, Los Angeles, CA, USA

MSEC2017-2942

MEASUREMENT OF THE MELT POOL LENGTH DURING SINGLE SCAN TRACKS IN A COMMERCIAL LASER POWDER BED FUSION PROCESS

J.C. Heigel, B.M. Lane
National Institute of Standards and Technology
Gaithersburg, MD, U.S.A.

ABSTRACT

This work presents high speed thermographic measurements of the melt pool length during single track laser scans on nickel alloy 625 substrates. Scans are made using a commercial laser powder bed fusion machine while measurements of the radiation from the surface are made using a high speed (1800 frames per second) infrared camera. The melt pool length measurement is based on the detection of the liquidus-solidus transition that is evident in the temperature profile. Seven different combinations of programmed laser power (49 W to 195 W) and scan speed (200 mm/s to 800 mm/s) are investigated and numerous replications using a variety of scan lengths (4 mm to 12 mm) are performed. Results show that the melt pool length reaches steady state within 2 mm of the start of each scan. Melt pool length increases with laser power, but its relationship with scan speed is less obvious because there is no significant difference between cases performed at the highest laser power of 195 W. Although keyholing appears to affect the anticipated trends in melt pool length, further research is required.

INTRODUCTION

Metal additive manufacturing (AM) processes, such as powder bed fusion (PBF), can produce high-value parts with unique geometries and features that can significantly reduce weight or increase the performance of the fabricated part. However, these processes are extremely sensitive to thermal effects. For instance, the shape of the melt pool, which is created with a high intensity energy source such as a laser, is greatly affected by the part geometry due to its ability to conduct heat from the melt pool [1]. The resulting melt pool size, temperature gradients surrounding it, and thermal history during the entire process directly impact the microstructure and material properties of the final part [2] as well as its residual stress and distortion [3]. The significance of temperature and melt pool size on metal AM processes requires thorough investigation using measurement and simulation.

A variety of methods are capable of measuring the thermal history during AM processes. Thermocouples have been used to measure the temperature at select points on parts during a variety of AM processes and those measurements have been used to validate process models [4], [5] and to investigate different processing strategies [6]. However, thermocouples have limited application in AM research because they must be attached to the substrate before the process begins, and can only measure temperature near the melt pool if the process is paused to allow additional thermocouples to be attached [4]. Optical methods, such as pyrometers or cameras, are more appealing than thermocouples because the melt pool and the surrounding material can be directly observed. Unfortunately, these too have their challenges. Pyrometers, for instance, collect radiation from a finite area (large or small) and convert that into a single value, from which a true temperature may or may not be calculable [7]–[9].

Thermal cameras unfortunately do not directly measure temperature; they provide signals nominally proportional to the incident radiant flux on each pixel. In order to convert thermal camera signal to true thermodynamic temperature, the measured object's emissivity must be known. However, emissivity of metals may vary with temperature, wavelength, viewing angle, surface condition, material phase, surface chemistry, and more [10], and thus true temperature profiles on and near the melt

Contact author: jarred.heigel@nist.gov

pool are very difficult to accurately measure. Fortunately, certain characteristics of the temperature profile can be attributed to known physical processes, namely, the solidification boundary of the melt pool. The exothermic reaction that occurs during the liquid to solid phase transformation causes the temperature to plateau during that transition, creating a discontinuity in the temperature profile. The camera signal corresponding to that discontinuity is then used to identify the melt pool boundary.

Several researchers have used the solidification boundary to measure melt pool geometry. For instance, Doubenskaia and colleagues used a mid-infrared camera to image the melt pool while laser cladding a titanium alloy (Ti-6Al-4V) using a laser to create a 2.5 mm wide spot into which powder was fed at a rate of 10.5 g/min [11]. They identified the liquidus-solidus transition in the temperature profile across the width of the melt pool. Other researchers have used the same approach to measure melt pool length during the PBF process, which has significantly smaller melt pool sizes compared to directed energy deposition processes, such as laser cladding. Price, Cheng, and their colleagues first demonstrated the capabilities of their infrared camera to measure the temperature and the liquidus-solidus transition during an electron beam PBF process [12], used those measurements to validate a finite element (FE) model [13], and then used the experimental method and model to investigate the impact of various processing conditions on the melt pool geometry [14]. Their measurement setup used a 60 Hz infrared camera that was mounted outside of the machine and tilted down 35° to observe a 31 mm by 23 mm area on the build surface. The melt pool length and width were shown to vary based on processing conditions. Instead of observing the melt pool from an angle outside of the build chamber, Yadroitsev and colleagues utilized a charge-coupled device (CCD) camera integrated into the optics of a laser PBF system to measure the melt pool while processing Ti-6Al-4V [15]. Once again the liquidus-solidus transition was prevalent and was used to identify the melt pool boundary.

Each of these studies that used the liquidus-solidus transition to identify the melt pool boundary was performed on titanium alloys, and used relatively slow camera speeds (frames per second) compared to the process scan speeds. High frame rates are required to measure the variability in the melt pool length over the distance it travels. Furthermore, there are no measurements of melt pool length on other materials relevant to AM processes, such as nickel alloys.

The objectives of this work are twofold: 1) to present the current capabilities at the National Institute of Standards and Technology (NIST) to measure process temperatures and melt pool lengths during powder bed fusion processes, and 2) to present melt pool length measurements for a variety of processing conditions on nickel alloy 625 (IN 625) substrates and to discuss their significance. An infrared camera is used to measure the emissions from single line laser scans on bare IN 625 substrates using a frame rate of 1800 frames per second. These measurements are performed on a commercial laser PBF system. The analysis of the measurement data is automated using an algorithm to detect the liquidus-solidus transition discontinuity and uses those results to measure the melt pool length. Results of this analysis are then compared to processing conditions and the results of other studies in the literature.

MEASUREMENT SETUP

Figure 1 shows the setup used in this study, which is an evolution of the one originally used by Lane and colleagues [16]. A custom door allows an infrared camera to be positioned as close and as perpendicular to the build surface as possible. The door is mounted to the same commercial laser PBF system, which uses a 200 W Yb-fiber laser to produce a 100 µm spot size on the surface of the substrate. This study also uses the same camera with a filter that only allows wavelengths between 1350 nm and 1600 nm to be detected. The integration time (shutter speed) of the camera is 40 µs and the frame rate is 1800 Hz. To achieve this frame rate, a limited window size is used (360 horizontal pixels, 128 vertical pixels). Considering the camera magnification of approximately 0.33x, a working distance of approximately 162 mm, and a relative angle between the camera and the target surface of 44°, the pixel resolution in the horizontal and vertical axes are 36 µm and 52 µm, respectively. This equates to a field of view (FOV) that is 12.96 mm wide and 6.82 mm tall.

A new calibration of the infrared camera is performed following the procedure outlined by Lane and Whitenton [17]. The following equation relates the camera signal (S, in digital levels, DL), to the temperature of a reference black body (T_{BB}):

$$T_{BB} = \frac{c_2}{A\, ln\left(C/S - 1\right)} - \frac{B}{A} \quad (1)$$

where c_2 is the second radiation constant (14338 µm/K) and the coefficients A, B, and C are determined by fitting the equation

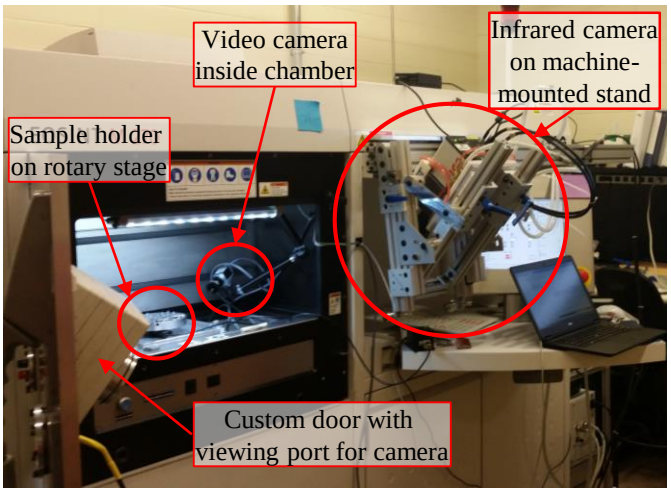

Figure 1 – Thermography setup on the commercial laser PBF system with the thermal camera set adjacent to the testing position and the custom door open, exposing the sample holder and video camera inside the chamber.

to the measurement. In this instance A=1.442, B=9.5×10^{-10}, and C=2.66×10^{7}. Figure 2 presents the black body measurements, the calibration curve, and the associated residuals. While this calibration can be used to measure the temperature of a black body to within a few degrees at high temperatures, it can only measure the radiant temperature of any object with an emissivity less than 1, as is the case in this study. Furthermore, the measurement uncertainty of this system is certainly higher than the reported residual since optical blur, motion blur, emissivity variation, and other potential components of measurement uncertainty must be measured individually, which is beyond the scope of this paper [16], [17].

In addition to the new camera calibration, several modifications are made to the setup to improve the quality and the quantity of measurements that can be made in a reasonable amount of time. First, the camera is attached to a new stand that is mounted directly to the machine, enabling the camera to be moved to allow the door to be opened and then repositioned so that it is focused on the same spot to within 1 mm. The second improvement is a sample holder mounted to a rotary stage that allows multiple samples to be loaded into the machine and indexed into the camera's field of view so that virgin sample surfaces can be scanned, as shown in Figure 3. This decreases the number of times the chamber door needs to be opened and closed, which requires time for the build chamber atmosphere to reach an environment with oxygen content less than 1 %.

In the current study, single line scans are made on square 3.2 mm thick IN 625 samples with a top surface area measuring 25.4 mm wide and 25.4 mm long. These samples are not pre-heated and have an initial temperature equal to the ambient temperature inside the build chamber (approximately 30 °C).

Table 1 presents the combinations and replications of laser scanning parameters investigated in this study. The laser power and scan speed are the programmed values. Combinations of these parameters are chosen based on the manufacturer recommended values for this material (Case 7) and the conditions investigated by Montgomery et al. in their study on the same machine [18]. The primary scan length for each case is 4 mm, though for some cases that length is increased to 8 mm and 12 mm to verify that steady state conditions are achieved.

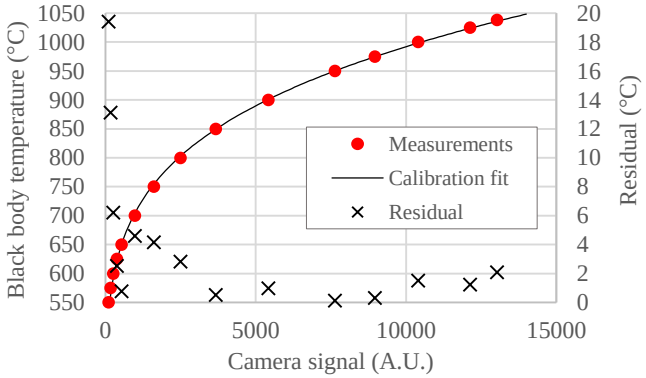

Figure 2 – Calibration results of the infrared camera.

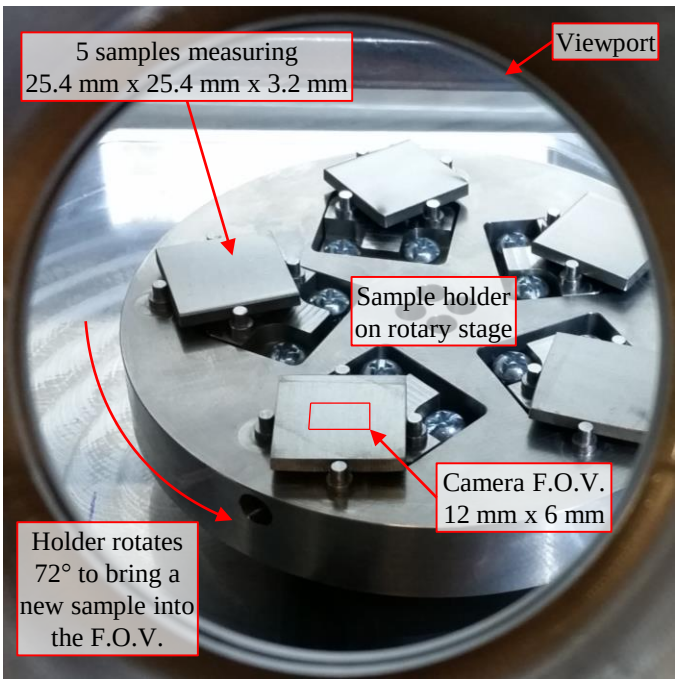

Figure 3 – The five samples held by the rotary stage as seen from the camera's perspective through the viewport on the custom door.

Table 1 – Test cases of varying laser power, scan speed, and scan length combinations.

Case	Power (W)	Speed (mm/s)	# of replications for scan lengths of: 4 mm	8 mm	12 mm
1	49	200	4	2	2
2	122	200	1	-	-
3	122	500	1	-	-
4	122	800	1	-	-
5	195	200	1	-	1
6	195	500	2	-	1
7	195	800	4	3	4

RESULTS

The infrared video by itself allows a qualitative analysis of the laser scan track; however, quantitative analysis is required to provide data and observations relevant to the research community. In the following sections, results from the infrared measurements are first shown, then the methodology used to analyze these results is developed, and finally the melt pool length measurements are presented.

The presentation of measurements in this study is limited to radiant temperature and the analysis of the data is focused on melt pool length because there is uncertainty surrounding the emissivity of the solidified material around the melt pool. The melt pool length can be measured without knowing true temperature using the liquidus-solidus transition, as demonstrated by other researchers [11]–[15].

Infrared Measurement Results

Figure 4 presents a typical infrared image from the steady state portion of each case. Steady state is defined in this work as the portion of a laser scan track during which the melt pool is fully developed and consistent. In most cases this is achieved after the laser has scanned over a distance between 1 mm and 2 mm, as will be shown later. In each image the laser scans from right to left and the leading edge of the 1038 °C radiant temperature isotherm (white), which is the highest measurable temperature of the camera using this calibration (Figure 2), is placed at the 0 mm mark on the horizontal axis to facilitate a quick, qualitative comparison between cases. A blue line indicates the center of the scan track. Each image shares the radiant temperature scale along the right side of the figure.

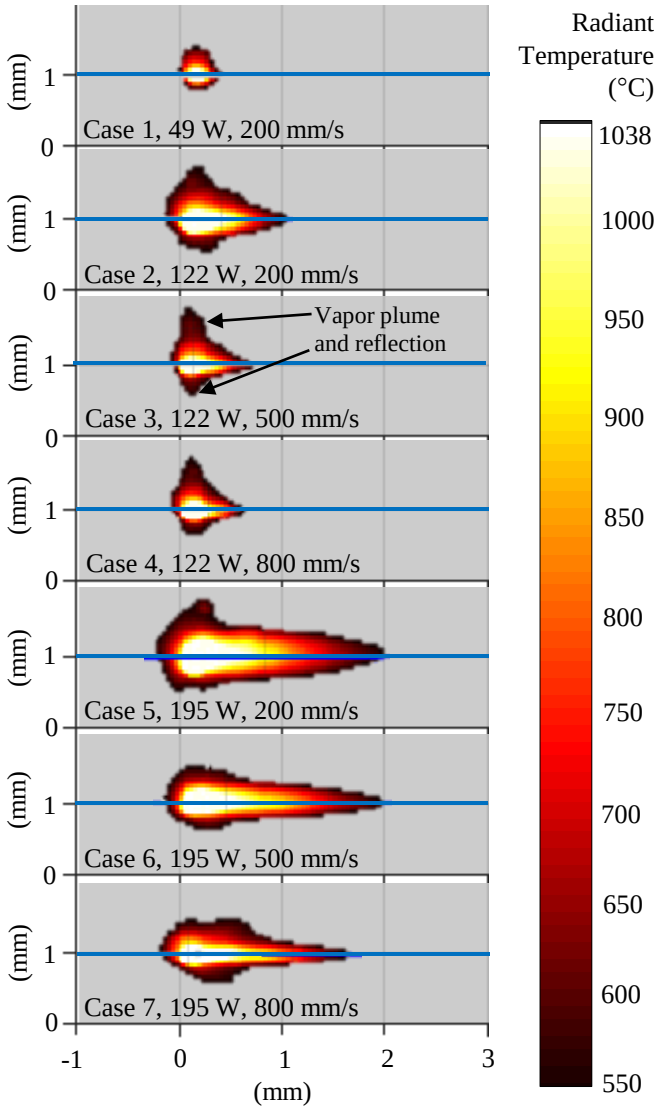

Figure 4 – A comparison of infrared images acquired from each case. Each image is representative of those acquired during steady state for each case. Temperatures below the detectable range of the camera (550 °C radiant) are gray.

The shape of these temperature gradients, especially those produced with higher laser powers, resembles those reported in other studies of laser scans using both experiment [9] and simulation [13], where it is wider in the front near the laser, and narrows behind the melt pool as the laser moves away and the material cools. Considering the similarity with these images and those in previous studies, caution must be exercised when interpreting these images due to the viewing angle of the camera and the vapor plume above the melt pool [19]. For instance, Case 3 in Figure 4 exhibits a plume above the melt pool that is reflected on the surface of the substrate (below the blue line). These plumes and their reflections, as well as the relatively large vertical scenel size (the area on the target that correlates to a single pixel), prevent any extraction of melt pool width from the data collected with this system.

Although no meaningful measurements can be made of the melt pool width, the melt pool length can be measured. Figure 5 presents the radiant temperature along the blue line for each infrared image shown in Figure 4. Once again, these plots are shifted along the horizontal axis so that the leading edges of the 1038 °C isotherm coincide, allowing easy comparisons.

The first observation that can be made from the curves in Figure 5 is that they are grouped by laser power. There is very little difference between Cases 5, 6, and 7, which all use a nominal laser power of 195 W. In each of those cases the 1038 °C radiant temperature isotherm is the same length (0.57 mm) and the cool down portions are similar, particularly Cases 5 and 6. Cases 3 and 4, which are created using the same nominal laser power of 122 W, are also very similar to each other (1038 °C isotherm length of 0.29 m and similar tails). However, Case 2 is longer even though it uses the same laser power of 122 W. The second observation pertains to the discontinuity in the cool-down portion of the temperature curves, particularly the ones generated with higher laser power. These discontinuities relate to the the liquidus-solidus transition observed by other researchers [11]–[15].

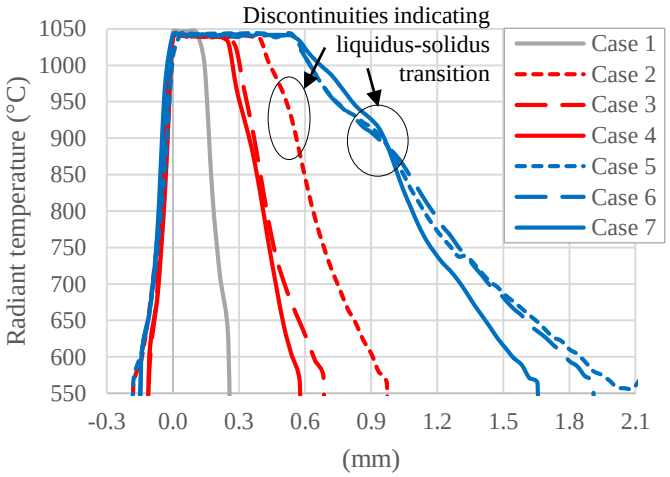

Figure 5 – Radiant temperature profile extracted along the blue lines in Figure 4.

Detection of the Liquidus-Solidus Transition

The presence of the discontinuity depends on the length of the temperature profile and the spatial resolution of the camera, as illustrated in Figure 6. This figure presents the temperature profiles to the right of (behind) the 1038 °C isotherms that were originally presented in Figure 5. For comparison's sake, the profiles have been shifted on the horizontal axis so their beginnings coincide. In addition, circles have been added to each plot to indicate every camera pixel used to measure the profile. As expected, the longer the distance over which the temperature decreases, the more pixels are able to measure it and the more evident the discontinuity becomes. For instance, if the transition is assumed (in this example) to occur at a radiant temperature of 900 °C for all cases, the numbers of pixels capturing data above and below that temperature (in Figure 6) are approximately 2 and 3 for Case 1, 4 and 10 for Cases 2 through 4, and 12 and 22 for Cases 5 through 7, respectively. Considering the subtle change in the temperature profile associated with the exothermic liquidus-solidus transition, it is impossible to detect when so few pixels are able to measure the gradient in Case 1, and is unreliable in Cases 2 through 4.

The average number of pixels (± 1 σ) above and below that hypothetical 900 °C radiant temperature threshold for every frame, during steady state of all replications, of each case, are presented in Table 2. The numbers in this table correspond well with the plots in Figure 6, indicating that those examples are representative of the steady state profiles of each case and further supporting the claim that the discontinuity cannot be adequately detected in Cases 1 through 4.

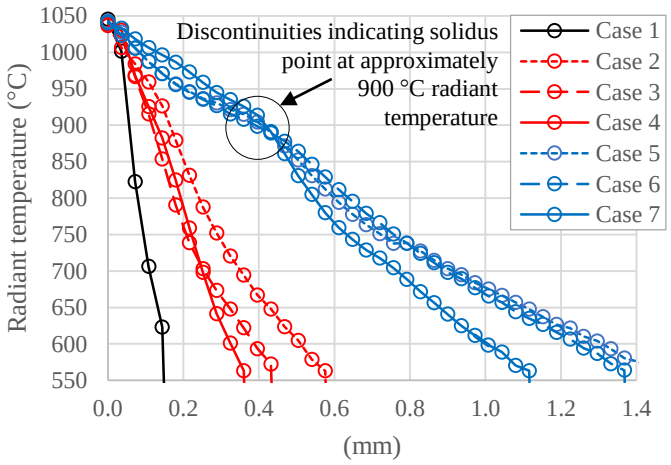

Figure 6 – The example temperature curves from Figure 5, isolated to the radiant temperature profile behind the 1038 °C isotherm.

Table 2 – Average number of frames and pixels available to use to detect the liquidus-solidus discontinuity.

Case	# of replications	Total # of frames	Average # of pixels between: 1038 °C to 900 °C	900 °C to 550 °C
1	8	503	0.8 ± 0.4	3.7 ± 0.5
2	1	15	3.7 ± 1.3	10.6 ± 4.1
3	1	10	3.0 ± 0.4	8.6 ± 1.6
4	1	6	2.8 ± 0.5	9.6 ± 3.5
5	2	144	10.2 ± 1.1	27.7 ± 4.6
6	3	54	10.7 ± 1.2	25.4 ± 2.3
7	11	151	10.1 ± 1.1	22.0 ± 2.6

Since there are a large number of frames to analyze (nearly 900), an algorithm is developed to identify the discontinuity. The minimum of the 2nd derivative of the temperature profile behind the 1038 °C radiant temperature isotherm is used to find the discontinuity, as shown in Figure 7. For each pixel the 1st and 2nd derivatives are calculated from a 3rd order polynomial that is fit to the measurement at that pixel and its 4 closest neighbors in that profile (5 total points).

Figure 8 shows the radiant temperatures of the discontinuity found in each frame of all Case 7 replications. These results are plotted against the approximate scan distance. In reality, the liquidus-solidus transition occurs over a constant (relatively narrow) temperature range that is dependent on the material and alloy [20]. However, the radiant temperature of this phenomena as measured by the infrared camera will be

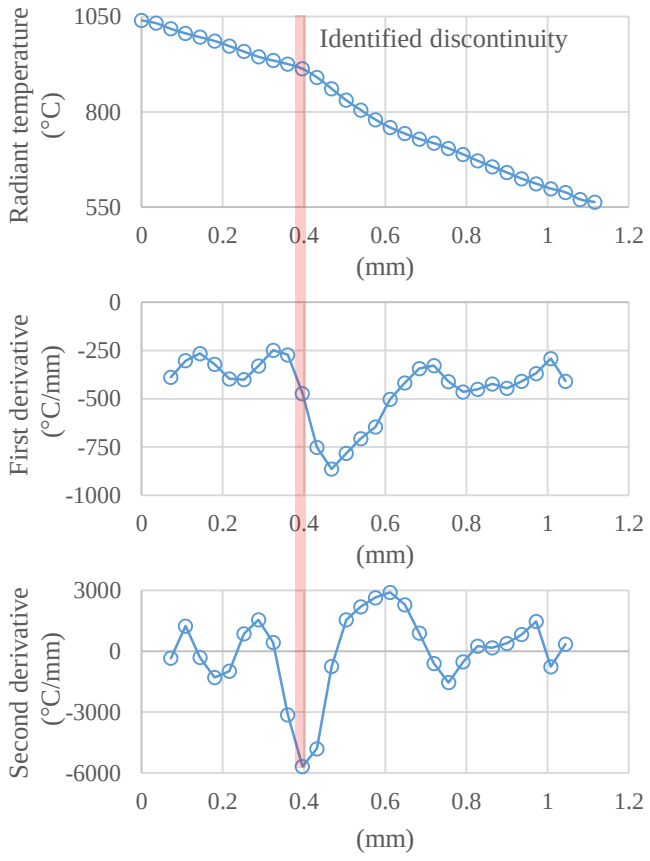

Figure 7 – An example of the algorithm used to detect the discontinuity at the liquidus-solidus transition. The radiant temperature profile is from the Case 7 profile presented in Figure 6. The minimum of the second derivative is used to identify the transition (vertical red line through each plot).

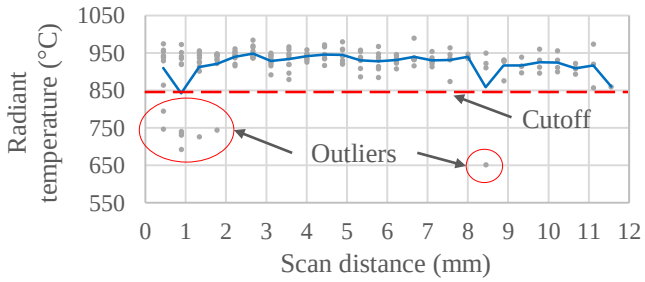

Figure 8 – The radiant temperature associated with the liquidus-solidus transition discontinuity in every frame for Case 7. Outliers are excluded from the analysis.

affected the emissivity, which is sensitive to the relative angle between the emitting surface and the camera [19]. Therefore, melt pool fluctuations could change this relative angle and make the discontinuity appear at different apparent temperatures. Interestingly, a greater number of outliers occur relatively close to the start of the scan, before a steady state melt pool can be achieved. Although worthy of investigation, an experimental investigation of these effects is currently not possible using the current setup due its magnification and frame rate.

Melt Pool Length Measurements

Once the radiant temperatures of all the discontinuities in every replication of a case are found, the outliers are rejected and the average is calculated. This average radiant temperature for each case is used to identify the leading and trailing edges of the melt pool for every replication of that case, enabling its length to be calculated. Since the temperature profiles in Cases 1 through 4 are too short to identify the discontinuity, an average radiant temperature is used which is calculated from Cases 5 through 7.

Table 3 presents the radiant temperatures used to identify the leading and trailing edges of the melt pool and the average melt pool length for each case. The variability of the radiant temperature is reported (± 1 σ), but is not considered when calculating the melt pool length. At this time, no analysis of the measurement uncertainty is performed, but will be a focus of future work. The melt pool data presented in Table 3 is the average length during steady state and its variability, ± 1 σ.

Figure 9 demonstrates the consistency in melt pool length measurements for all of the highest power cases (Case 5 through 7) and the distance traveled before reaching steady state. The average steady state length and the variability (± 1 σ) are represented by the solid and dashed black lines. Replications performed with different scan lengths are differentiated with markers of varying shapes and colors. These plots show that each replication within a certain case quickly converges to a steady state melt pool length after a short distance, making replications performed with different scan lengths indistinguishable. In the cases presented in Figure 9, steady state is achieved between 1 mm and 2 mm of travel, though there are a few exceptions that will be discussed shortly. The rapid increase in melt pool length to a steady state value, with no discernable difference between replications using different scan lengths, is observed in all other cases. Since the steady state melt pool length is unaffected by scan length (as long as the length is sufficiently long to achieve steady state), it is legitimate to average all steady state melt pool lengths, as they are reported in Table 3.

Table 3 – Results of the steady state melt pool analysis, average values and variabilities ± 1 σ.

Case	Power (W)	Speed (mm/s)	Radiant temperature used for detection (°C)	Melt pool length (µm)
1	49	200	942 ± 25	171 ± 16
2	122	200	942 ± 25	519 ± 29
3	122	500	942 ± 25	361 ± 27
4	122	800	942 ± 25	315 ± 27
5	195	200	961 ± 33	824 ± 109
6	195	500	949 ± 26	903 ± 102
7	195	800	936 ± 22	813 ± 79

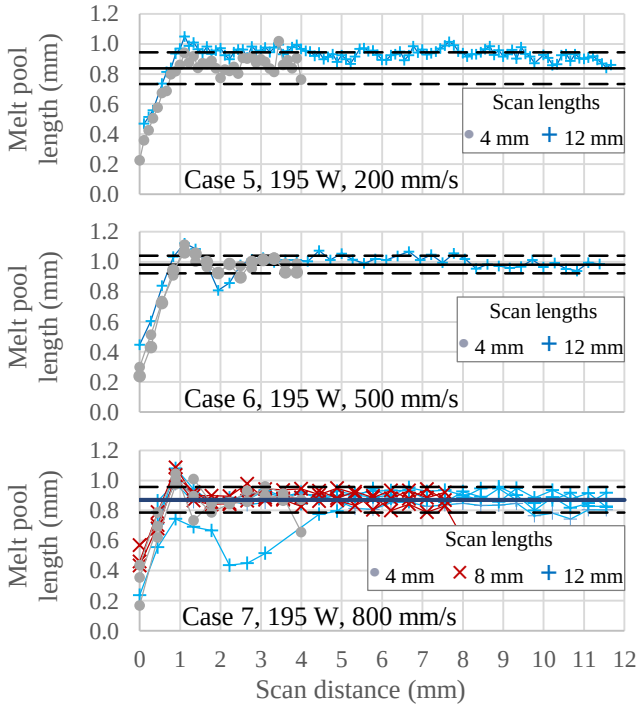

Figure 9 – Melt pool length as a function of laser scan distance for Cases 5, 6, and 7. The black solid line represents the average melt pool length during steady state while the black dashed lines are ± 1 σ.

There are a few outliers in the data presented in Figure 9. For instance, the final melt pool length measurement of some replications drops significantly below the steady state average. Analysis of these videos suggests that this is due to the final frame being captured after the laser is shut off and before the melt pool solidifies. The automated analysis algorithm used in this study cannot precisely determine the beginning and end of each scan because there is currently no signal from the machine to the data acquisition system indicating when the laser is on.

A few other replications do not follow the trend of the melt pool length rapidly increasing then becoming steady after a millimeter or two. For example, a few replications in Case 6 oscillate a bit before achieving steady sate. A more extreme instance occurs in Case 7, where one case nearly approaches steady state after 1 mm of travel, decreases in length over the next millimeter, and then increases and finally reaches steady state after another 3 mm of travel. Careful analysis of this video does not reveal any apparent cause for this behavior.

DISCUSSION

Figure 10 compares the average melt pool length for each case. Cases using the same nominal laser power are labeled to aid in the comparison of these measurements. This figure shows that melt pool length is closely related to the nominal laser power. Interestingly, the relationship with scan speed is less clear. According to the literature, the melt pool length is expected to decrease as the scan speed increases, though this relationship is expected to exponentially decay [9]. Cases 2 through 4 (122 W) exhibit this behavior; however, Cases 5 through 7 (195 W) do not. There is no significant difference between the three cases using the highest power.

The insensitivity of melt pool length to scan speed during the highest laser power cases (5 through 7) may be explained when considering the keyholing regime identified in an earlier study [18] and presented in Figure 11. This figure presents the power and velocity (P-V) map for IN 625 for the specific PBF machine used in the current study. The earlier study established lines of constant melt pool cross sectional area and the shaded region in which keyholing was observed [18]. The representative thermal images of each case from the current study are superimposed. Case 5 is well within the keyholing regime while Case 6 is near the transition into that regime. It is possible that the occurrence and extent of keyholing reduces the melt pool length, possibly due to the extra energy that is

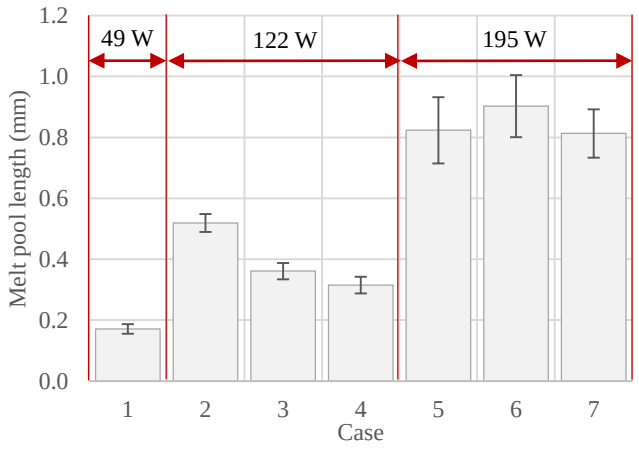

Figure 10 – Comparison of the melt pool lengths of each case. Cases with the same nominal laser power are grouped together to highlight the similarities in melt pool length. Error bars represent measurement variance of ± 1 σ.

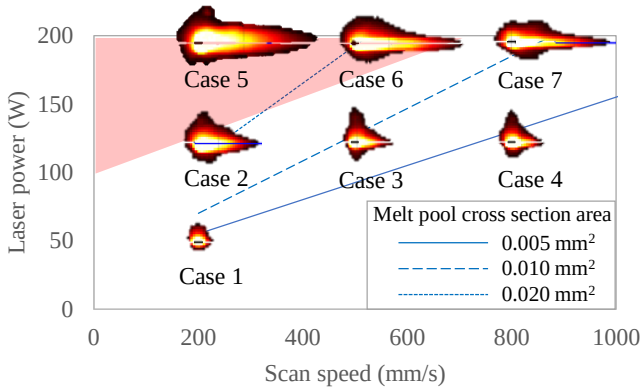

Figure 11 – The representative images and average melt pool length measurement mapped onto the P-V space. The shaded region in the upper left hand corner indicated where keyholing is expected according to Montgomery et al. [18].

expelled by the melt pool from ejected particles or from the deeper penetration of the melt pool, enabling the heat to be conducted deeper into the substrate compared to cases when keyholing does not occur.

The data shown in Figure 11 and Table 3 show that melt pool length increases along lines of constant melt pool cross section as the power and speed increase [18]. For instance, Cases 1 and 4 lie (nearly) on the same cross section line (0.005 mm^2) and the increase in power and speed from Case 1 to 4 increases the melt pool length from 171 µm to 315 µm (an increase of 84 %). Similarly, the melt pool length of Case 6 is 76 % greater than Case 2, while they both approximately fall on the 0.020 mm^2 line. More dramatically, along the 0.010 mm^2 cross section line, the melt pool length increases from Case 3 to Case 7 by 125 %. These results are consistent with the literature, since the length to depth ratio along those lines is expected to increase [18].

CONLCUSIONS

This work presents thermographic measurements of single track laser scans made using a commercial laser PBF machine on IN 625 plates. Infrared images acquired at a rate of 1800 frames per second are used to measure the temperature gradients in and around the melt pool. A variety of speed and power combinations are investigated using a number of replications performed at varying lengths. These power and speed combinations are based on earlier P-V mapping work on the same machine used in this study [18].

The melt pool length is measured from these gradients using the radiant temperature of the solidus transition. This transition manifests itself in the measured temperature gradients as a plateau in the curve which is caused by the release of energy during the solidification process and has been used by other researchers to identify the melt pool boundary. The true temperature gradient is not calculated in this study due to the unknown emittivity of the IN 625 surface at the observed temperatures and surface conditions.

Results from this study indicate that the melt pool length of single scan lines typically stabilizes within 1 mm to 2 mm of the start of the scan, reaching a steady state value that is strongly related to the nominal laser power. In contrast, the relationship with scan speed is less clear. Lower power cases (122 W) show a slight decrease in length with increasing scan speed, while the highest power cases (195 W) show no significant difference in length over the investigated scan speed range from 200 mm/s to 800 mm/s. Keyholing, which is expected to occur at the combination of high power and lower speed, possibly decreases the melt pool, negating the anticipated relationship between speed and melt pool length. Finally, the length of a melt pool does not correlate with its cross sectional area. Most of these observations are consistent with the literature.

Future work using this experimental setup and melt pool length measurement methodology will further investigate the effects in the keyholing region and the impact of the heat accumulated from successive scans on the melt pool length.

REFERENCES

[1] A. Vasinonta, J. L. Beuth, and R. Ong, "Melt pool size control in thin-walled and bulky parts via process maps," *Solid Freeform Fabrication Symposium Proceedings*, pp. 432–440, 2001.

[2] N. Hrabe and T. Quinn, "Effects of processing on microstructure and mechanical properties of a titanium alloy (Ti–6Al–4V) fabricated using electron beam melting (EBM), part 1: Distance from build plate and part size," *Materials Science and Engineering: A*, vol. 573, pp. 264–270, 2013.

[3] A. Dunbar *et al.*, "Experimental In Situ Distortion and Temperature Measurements During the Laser Powder Bed Fusion Additive Manufacturing Process. Part 1: Development of Experimental Method," *Additive Manufacturing*, 2016.

[4] J. C. Heigel, P. Michaleris, and E. W. Reutzel, "Thermo-mechanical model development and validation of directed energy deposition additive manufacturing of Ti–6Al–4V," *Additive Manufacturing*, vol. 5, pp. 9–19, 2015.

[5] A. J. Dunbar, E. R. Denlinger, M. F. Gouge, and P. Michaleris, "Experimental validation of finite element modeling for laser powder bed fusion deformation," *Additive Manufacturing*, vol. 12, pp. 108–120, 2016.

[6] E. R. Denlinger, J. C. Heigel, P. Michaleris, and T. A. Palmer, "Effect of inter-layer dwell time on distortion and residual stress in additive manufacturing of titanium and nickel alloys," *Journal of Materials Processing Technology*, vol. 215, pp. 123–131, Jan. 2015.

[7] M. Doubenskaia, M. Pavlov, S. Grigoriev, E. Tikhonova, and I. Smurov, "Comprehensive optical monitoring of selective laser melting," *Journal of Laser Micro Nanoengineering*, vol. 7, no. 3, pp. 236–243, 2012.

[8] C.-H. Cho, Y.-C. Hsieh, and H.-Y. Chen, "Welding pool measurement using thermal array sensor," 2015, vol. 9609, pp. 960912-960912–7.

[9] J.-P. Kruth, P. Mercelis, J. Van Vaerenbergh, and T. Craeghs, "Feedback control of selective laser melting," presented at the Proceedings of the 3rd International Conference on Advanced Research in Virtual and Rapid Prototyping, 2007, pp. 521–527.

[10] Y. S. Touloukian and D. P. DeWitt, "Thermophysical Properties of Matter - the TPRC Data Series. Volume 7. Thermal Radiative Properties - Metallic Elements and Alloys," 1970.

[11] M. Doubenskaia, M. Pavlov, S. Grigoriev, and I. Smurov, "Definition of brightness temperature and restoration of true temperature in laser cladding using infrared camera," *Surface and Coatings Technology*, vol. 220, pp. 244–247, 2013.

[12] S. Price, J. Lydon, K. Cooper, and K. Chou, "Experimental temperature analysis of powder-based electron beam additive manufacturing," *Solid Freeform Fabrication Symposium Proceedings*, pp. 162–173, 2013.

[13] B. Cheng, S. Price, J. Lydon, K. Cooper, and K. Chou, "On Process Temperature in Powder-Bed Electron Beam Additive Manufacturing: Model Development and Validation," *Journal of Manufacturing Science and Engineering*, vol. 136, no. 6, p. 61018, 2014.

[14] S. Price, B. Cheng, J. Lydon, K. Cooper, and K. Chou, "On Process Temperature in Powder-Bed Electron Beam Additive Manufacturing: Process Parameter Effects," *Journal of Manufacturing Science and Engineering*, vol. 136, no. 6, p. 61019, 2014.

[15] I. Yadroitsev, P. Krakhmalev, and I. Yadroitsava, "Selective laser melting of Ti6Al4V alloy for biomedical applications: Temperature monitoring and microstructural evolution," *Journal of Alloys and Compounds*, vol. 583, pp. 404–409, 2014.

[16] B. Lane, S. Moylan, E. Whitenton, and L. Ma, "Thermographic Measurements of the Commercial Laser Powder Bed Fusion Process at NIST," *Rapid Prototyping Journal*, vol. 22, no. 5, pp. 778-787, 2015.

[17] B. Lane and E. Whitenton, "Calibration and measurement procedures for a high magnification thermal camera," National Institute of Standards and Technology, Gaithersburg, MD, NISTIR 8098, Dec. 2015.

[18] C. Montgomery, J. Beuth, L. Sheridan, and N. Klinbeil, "Process mapping of Inconel 625 in laser powder bed additive manufacturing," *Solid Freeform Fabrication Symposium Proceedings*, pp. 1195–1204, 2015.

[19] S. A. Khairallah, A. T. Anderson, A. Rubenchik, and W. E. King, "Laser powder-bed fusion additive manufacturing: Physics of complex melt flow and formation mechanisms of pores, spatter, and denudation zones," *Acta Materialia*, vol. 108, pp. 36–45, 2016.

[20] L. del Campo *et al.*, "Emissivity measurements on aeronautical alloys," *Journal of Alloys and Compounds*, vol. 489, no. 2, pp. 482–487, Jan. 2010.